scientific reports

Check for updates

OPEN

New functions of B9D2 in tight junctions and epithelial polarity

Chloe Caenen-Braz[1], Latifa Bouzhir[1] & Pascale Dupuis-Williams[1,2]✉

Ciliopathies are a diverse group of disorders resulting from abnormalities in the development or function of multiple organs. While significant research has clarified the role of the primary cilium in transducing numerous signalling pathways, elucidating causes of neuronal and skeletal development disorders, the origins of other ciliopathy-related conditions, such as hepatic fibrocystic diseases, remain elusive. Additionally, attempts to correlate specific ciliary proteins with distinct phenotypes have been largely unsuccessful due to the variable and overlapping symptoms of ciliopathies. This study aims to elucidate the extraciliary roles of the protein B9D2 in the development of biliary dysgenesis, a condition present in Meckel-Gruber and Joubert syndromes caused by mutations in this protein. Traditionally, B9D2 is known for its role at the transition zone of the primary cilium in the transduction of signalling pathways notably Wingless and Hedgehog. Our work demonstrates that before ciliogenesis occurs, B9D2 is crucial for the maturation and maintenance of tight junctions ensuring epithelial barrier tightness and appropriate biliary lumen formation. This study provides new insights into the mechanisms underlying biliary dysgenesis in hepatic ciliopathies, suggesting that further exploration of the non-ciliary functions of proteins involved in ciliopathies could lead to a better understanding and treatment of these complex disorders.

Keywords Ciliopathy, B9 domain proteins, Tight junctions, Bile ducts morphogenesis

B9 domain proteins are crucial components of the primary cilium implicated in Meckel-Guber (MKS)[1,2], Joubert[3] and Bardet-Biedl ciliopathies[4]. Such diseases arise from dysfunction of the primary cilium, the "cellular antenna" for transmission of external biochemical, osmotic and mechanical signals[5,6]. The hallmark features of these ciliopathies include developmental abnormalities of the central nervous system, polycystic kidneys, liver malformations and polydactyly[7,8].

Our research focuses on liver anomalies observed in MKS and Joubert syndromes, stemming from mutations in B9 domain proteins. These fibrocystic diseases belong to the DPM (Ductal Plate Malformations) hepatic diseases. During embryogenesis, the Ductal Plate (DP) which forms rings around the portal veins is remodeled along the vasculature to form an interconnected network of bile ducts[9,10]. Patients with MKS or Joubert syndrome exhibit multiple dilated and mispositioned biliary ducts, with the presence of cysts often associated with liver fibrosis[3,7].

B9 domain proteins are ciliary proteins evolutionarily conserved across ciliated eukaryotes[11]. Among them, the B9 domain containing 2 protein (B9D2) is a 19kDa protein (UniProt Q9BPU9) belonging to the MKS complex located at the transition zone of the primary cilium. At this site, the localization of the three B9 domain proteins (MKS1-B9D1-B9D2) is interdependent with B9D2 anchoring both MKS1 and B9D1, leading to a linear complex[12]. The MKS complex controls ciliogenesis and acts as a diffusion barrier, regulating proteins entry into the primary cilium[13–15]. Notably, B9 domain proteins play essential roles in Hedgehog and Wingless signaling pathways[16,17], elucidating brain and kidney anomalies observed in patients. However, the numerous studies aimed at identifying the phenotypic consequences of mutations or null alleles of transition zone proteins including the MKS module have led to unclear results. Thus, whilst conditional loss of B9D2 in the nervous system and kidneys of mice leads to hydrocephalus and renal cysts[18], zebrafish carrying B9D2 mutations do not exhibit kidney defects but display skeletal abnormalities, juvenile mortality, infertility, and retinal degeneration[1,19]. In human, investigations into potential liver defects with B9D2 loss of function remain scarce. The sequencing on large cohorts of Joubert[3] or Meckel[1,2] syndromes have identified B9D2 mutation leading to DPM. Many cholangiopathies result from DPM, often due to specific genetic defects in proteins not exclusively expressed in the primary cilium. In cases of acquired liver damage, liver repair processes mimic developmental mechanisms. Understanding developmental diseases of the biliary system therefore opens up broader perspectives for the treatment of chronic biliary diseases or in the context of regenerative medicine[20]

[1]Université Paris-Saclay, Inserm, physiopathogenèse et traitement des maladies du foie, 94800 Villejuif, France. [2]ESPCI Paris, Université PSL, 75005 Paris, France. ✉email: pascale.dupuis-williams@universite-paris-saclay.fr

It is well-established that several ciliary proteins play extraciliary functions in epithelial cells[21]. This holds true for ciliary proteins of the transition zone, such as nephrocystins like NPHP1 shown to be localized at adherens junctions and focal adhesions, NPHP2 (Inversin) to the nucleus and adherens junctions and NPHP4 which interacts with β-catenin at cell junctions[22–24].

In this paper, with the aim of better understanding the etiology of the liver ciliopathies, we investigated the extraciliary functions of the transition zone protein B9D2 in tight junction (TJ) maturation and in the establishment of epithelial polarity.

Results

Extraciliary localization of B9D2 at cell junctions

We first sought to identify the subcellular localization of the B9D2 protein during the acquisition of epithelial polarity, in two epithelial cell models: a cholangiocyte cell line (NRC) and a kidney epithelial cell line (NRK) chosen for their distinct kinetics of epithelial polarity and ciliogenesis under our culture conditions (see Materials and Methods). For this purpose, cells were seeded at increasing densities and observed after 5 days (NRC) or 1 day (NRK) respectively, corresponding to the time required for the cells to reach respectively 30%, 50%, 90% or full confluency. Both cell lines were cultured in serum to maintain them in a proliferative state to prevent primary cilium formation; preliminary experiments having shown that maintaining cultures in the presence of serum kept the rate of ciliated cells below 5% in confluent monolayers of NRK and of NRC, respectively after one day (1D) and 5D after reaching confluence.

B9D2 immunostaining was then carried out in these culture conditions (Fig. 1). In both cell lines, B9D2 predominantly localized at the plasma membrane between adjacent cells and near the nucleus in incompletely polarized cells. This membrane localization of B9D2 occurred upon cell contact establishment, coinciding with the formation of cell junctions. B9D2 co-localized with ZO1 throughout the epithelium formation and cell polarization. Furthermore, after ciliogenesis induction by serum deprivation in confluent NRC and NRK cultures, the dual localization of B9D2 to tight junctions (TJ) and the cilium suggests the possibility of a cilium-independent function of B9D2 at TJ during the establishment of epithelial polarity in both cholangiocytes and renal epithelial cells (Supplementary Fig. S1).

To ascertain a potential extraciliary localization of B9D2, immunofluorescence co-labelling experiments were performed with several junctional proteins in confluent NRC (Fig. 2) belonging respectively to the TJ: ZO1 and Claudin 4; the adherens junctions: E-Cadherin and β-catenin; and the desmosomes: Plakoglobin. Confocal microscopy revealed colocalization of B9D2 with ZO1 (Fig. 2A) and Claudin 4 (Fig. 2B), as indicated by Manders coefficient $M2 > 0.7$. The $M1 < 0.5$ coefficient supporting our first observation that B9D2 is split between cytosolic localization and the cell junctions. Conversely, B9D2 did not colocalize with adherens junction proteins E-cadherin (Fig. 2C) and β-catenin (Fig. 2D), nor with the desmosomal protein Plakoglobin (Fig. 2E) asserted by Manders coefficients < 0.5. These results suggest that B9D2 is specifically localized at the TJ in NRCs.

B9D2 localizes with ZO1 and Claudin 4 at tight junctions

With the aim of further characterizing the location of B9D2 at the TJ, we investigated the relative position of B9D2 in relation to the cytosolic TJ protein ZO1 or the transmembrane protein Claudin 4. B9D2-ZO1 and B9D2-Claudin 4 co-labelling were analyzed using super-resolutive Structured Illumination Microscopy (Fig. 3). The NRCs were imaged from the apical to the basal pole (Fig. 3A). The focal planes along the z axis indicate that B9D2 (Fig. 3B1) is located together with ZO1 over a larger area than with Claudin 4 (Fig. 3C1), whose signal is detected in only one of the focal sections, 100 nm apart. By precise observation of the colocalization of B9D2 with respect to the two proteins on the focal planes (Figs. 3B2, C2), we observe that while ZO1 is uniformly distributed along the junction, B9D2 and Claudin 4 show a punctiform distribution, with signals spaced at approximately 300 nm for B9D2 and 500 nm for Claudin 4, as can be deduced from the plot profiles in Fig. 3B4, C4 respectively. Regarding the positioning of B9D2 with respect to the cell membrane, it appears that while B9D2 and ZO1 overlap perfectly over a width of about 1 µm as seen in the plot profile of the cross section (Fig. 3B3), B9D2 and Claudin 4 immunostaining only partially overlap (Fig. 3C3). Altogether, these results reveal that B9D2 is closer to the cytosolic protein ZO1 than to the transmembrane protein Claudin 4.

Function of B9D2 in tight junctions' structure

We then explored the possible function of B9D2 in intercellular junction composition by studying the localization of tight or adherens junction proteins in shRNA-induced knockdown cells. Confluent NRCs were transfected with shRNAs (Ctrl or B9D2: see Materials and Methods) fused to RFP, allowing shRNA expressing cells to be identified by a red fluorescent signal in both cases. The average decrease in B9D2 expression in NRC epithelia was assessed by western blot (Supplementary Fig. S2B). These cells were then immunolabeled with various cell junction proteins to assess the influence of B9D2 knockdown on the establishment and maintenance of these junctions.

Whereas the staining of catenins (β-catenin: Fig. 4D and Plakoglobin: Fig. 4E) remain unchanged in shB9D2-expressing cells compared to control cells (shCtrl transfected), the knockdown of B9D2 induced a modification of the expression of ZO1 and even more notably of the localization of Claudin 4 (Fig. 4B) and E-cadherin (Fig. 4C). Compared to the control NRC epithelia (shCtrl transfected) where ZO1 labelling is drawing a thin line surrounding the cells (Fig. 4A), it appears thicker in the shB9D2 transfected epithelia and partly discontinuous (Fig. 4A, F). This qualitative analysis was confirmed by the quantification of the ZO1 immunofluorescence across the junctions which extends over 2 µm in the B9D2 knockdown cells rather than 1µm in the control cells (Supplementary Fig. S3). Moreover, the calculation of the ratio of membrane over juxtamembrane cytosolic fluorescent signals calculated from RFP positive shRNA expressing cells confirms that the intensity

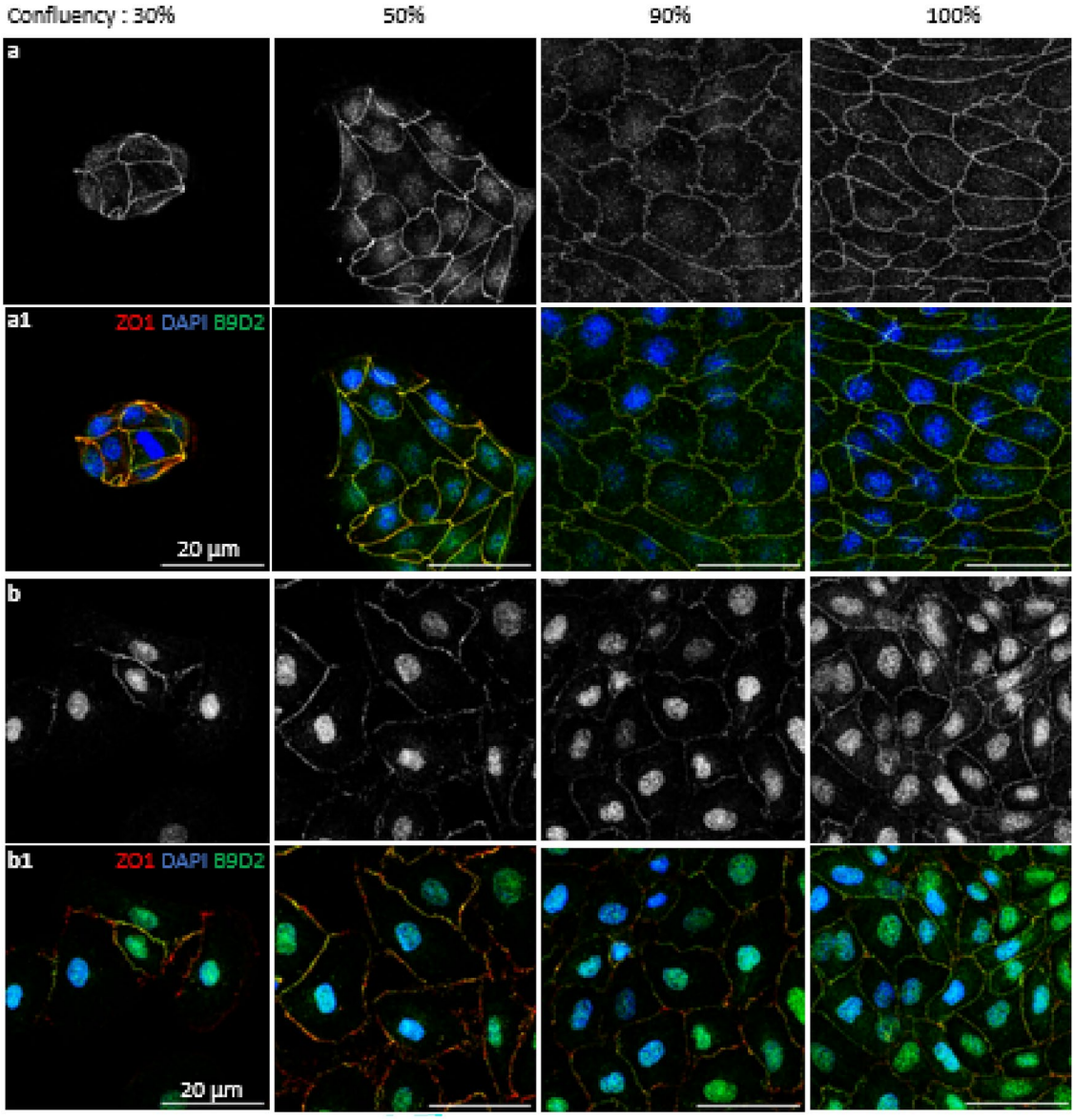

Fig. 1. B9D2 subcellular localization during epithelial polarization. Co-Immunostaining of B9D2 and ZO1 during epithelial polarization. Cells were seeded at growing densities and observed after 5 days (NRC) or 1 day (NRK) until reaching 30%-50%-90%-100% confluency (left to right). Both cell types were maintained in culture with serum in order to keep the amount of ciliated cells below 5% in confluent monolayers. Maximal intensity projection of confocal images of B9D2 (**a**, **b**) or merge B9D2/ZO1 (**a1**, **b1**) of NRC (**a**, **a1**) or NRK (**b**, **b1**) cells.

of immunofluorescence is more concentrated at the intercellular membrane of the Ctrl cells than in the B9D2 knockdown cells (Supplementary Fig. S3B).

B9D2 knockdown effect was even stronger on the localization of Claudin 4 and E-cadherin whose immunostaining, rather than lining the intercellular junctions like in control cells (Fig. 4B, C) appears greatly reduced at the cell junctions and rather scattered over a larger zone around the intercellular membrane (Supplementary Fig. S3A and S3B).

As a result of the knockdown effects summarized in Fig. 4F, B9D2 appears to be essential for the compaction of ZO1 in contact with the plasma membrane and for the targeting of the transmembrane proteins Claudin 4 and E-cadherin to the lateral cell junctions. These findings highlight the role of B9D2 in maintaining the integrity and organization of TJ.

B9D2's function in tight junctions' maturation

To further decipher the role of B9D2 in TJ establishment, we then looked at the effect of the knockdown of B9D2 on the structure of TJ using transmission electronic microscopy (TEM). The shCtrl- or shB9D2-transfected NRK cells, chosen for their ability to achieve more than 80% transfection efficiency (Supplementary Fig. S2C)

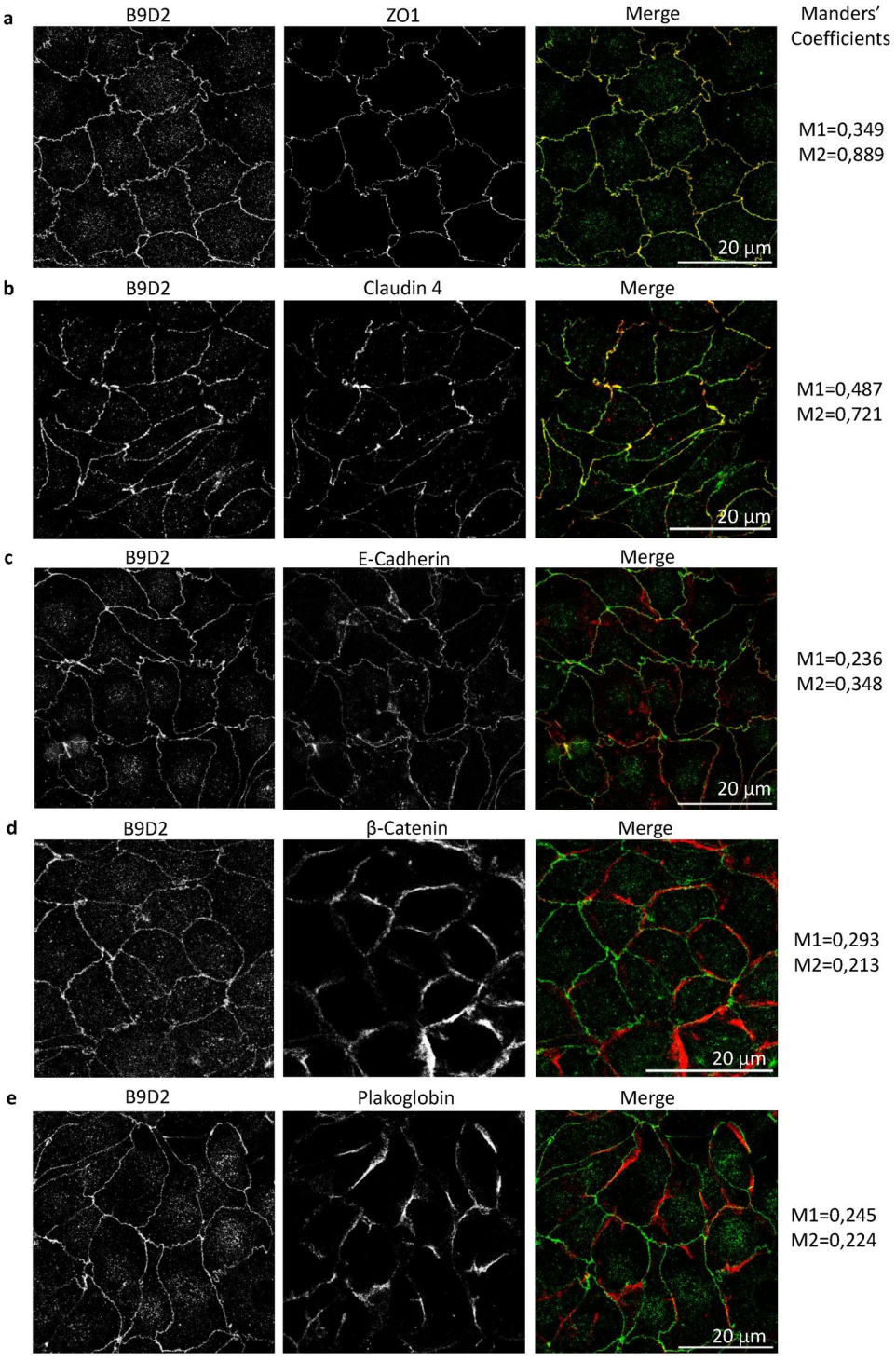

Fig. 2. B9D2 localizes at tight junctions. Co-immunostaining of B9D2 and junction proteins in NRCs confluent monolayers cultured in serum and fixed before ciliogenesis occurs (cilia rate below 5%; see Materials and methods). Focal plane of (**a**)/ ZO1, (**b**)/ Claudin 4, (**c**)/ E-cadherin, (**d**)/ β-catenin, (**e**)/ Plakoglobin (red), with B9D2 (green). The colocalisation Manders' coefficients: M1 (fraction of B9D2 overlapping with X) and M2 (fraction of X overlapping with B9D2) are indicated on the right of each double immunostaining.

were cultured to confluency, before being fixed and prepared for TEM imaging (Fig. 5A). Observation of the sections enabled us to classify the TJ into 4 stages of TJ maturation according to their structural characteristics and the organization of the intercellular spaces (Fig. 5B). The TJ appear as a black contrast between adjacent cells. Stage 1 corresponds to pre-TJ which appear as a contact point followed by large intermembrane spaces. Stage 2 corresponds to the reduction of the intermembrane spaces. Stage 3 groups elongated pre-TJ with polarization

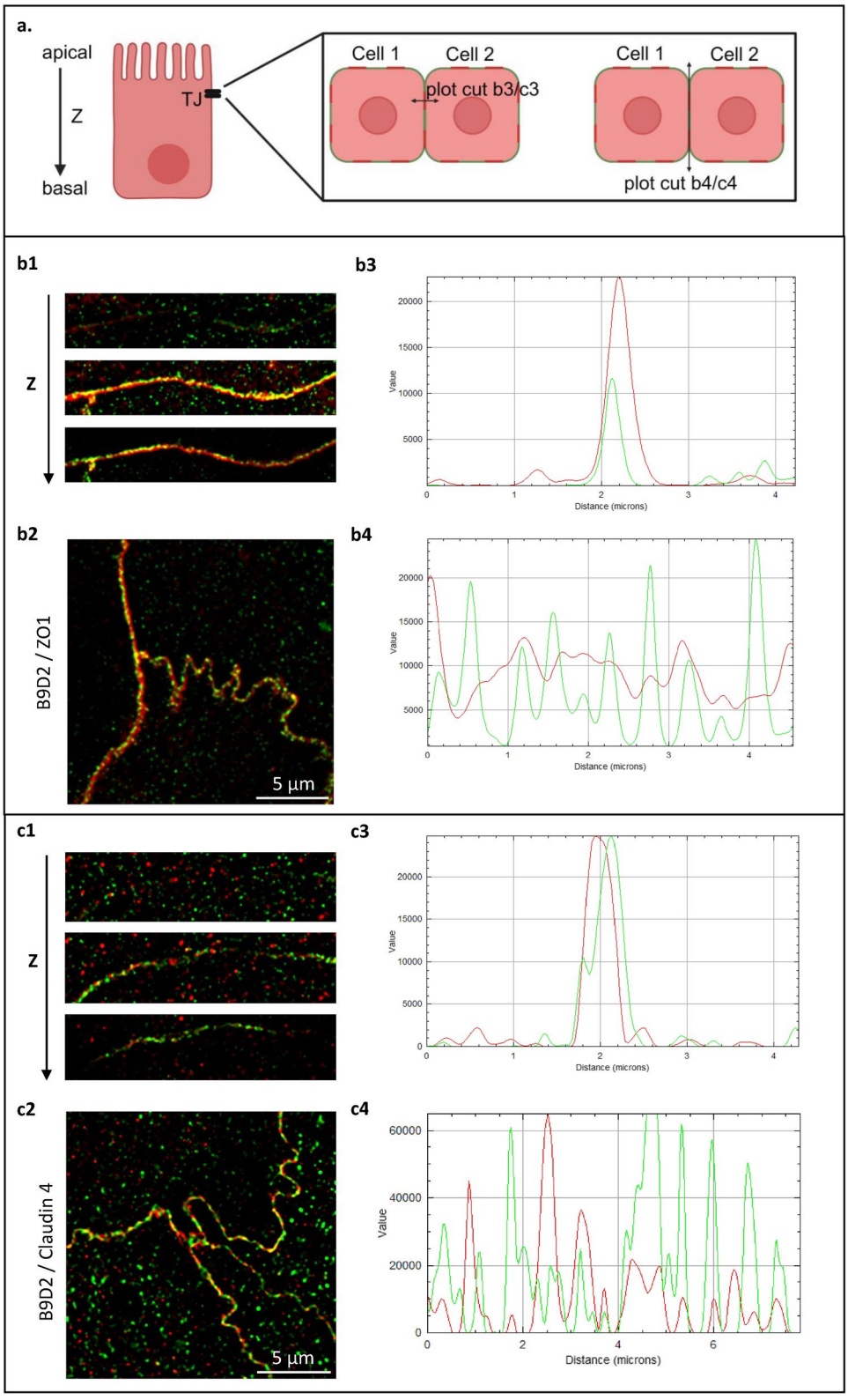

Fig. 3. Location of B9D2 with respect to TJ membrane. Co-immunostaining of B9D2 and tight junctions proteins (ZO1, Claudin 4) in polarized NRC epithelial cells. (**a**)/ Diagram showing the orientations of focal slices (cross section and along the TJ) and corresponding multichannels profile cuts (respectively **b3**,**c3** and **b4**,**c4**). Panel (**b**)/ B9D2 (green) and ZO1 (red) co-staining. Panel (**c**)/ B9D2 (green) and Claudin 4 (red) co-staining. For each co-staining, the positioning of B9D2 relative to ZO1 (**b**) or Claudin 4 (**c**) was examined along the z –axis (**b1**, **c1**) or on the XY focal plane (**b2**, **c2**). **b3**, **c3**: Histograms of fluorescence intensity of B9D2 (green) and ZO1 or Claudin 4 (red) across the TJ. **b4**, **c4**: Histograms of fluorescence intensity of B9D2 (green) and ZO1 or Claudin 4 (red) along the TJ.

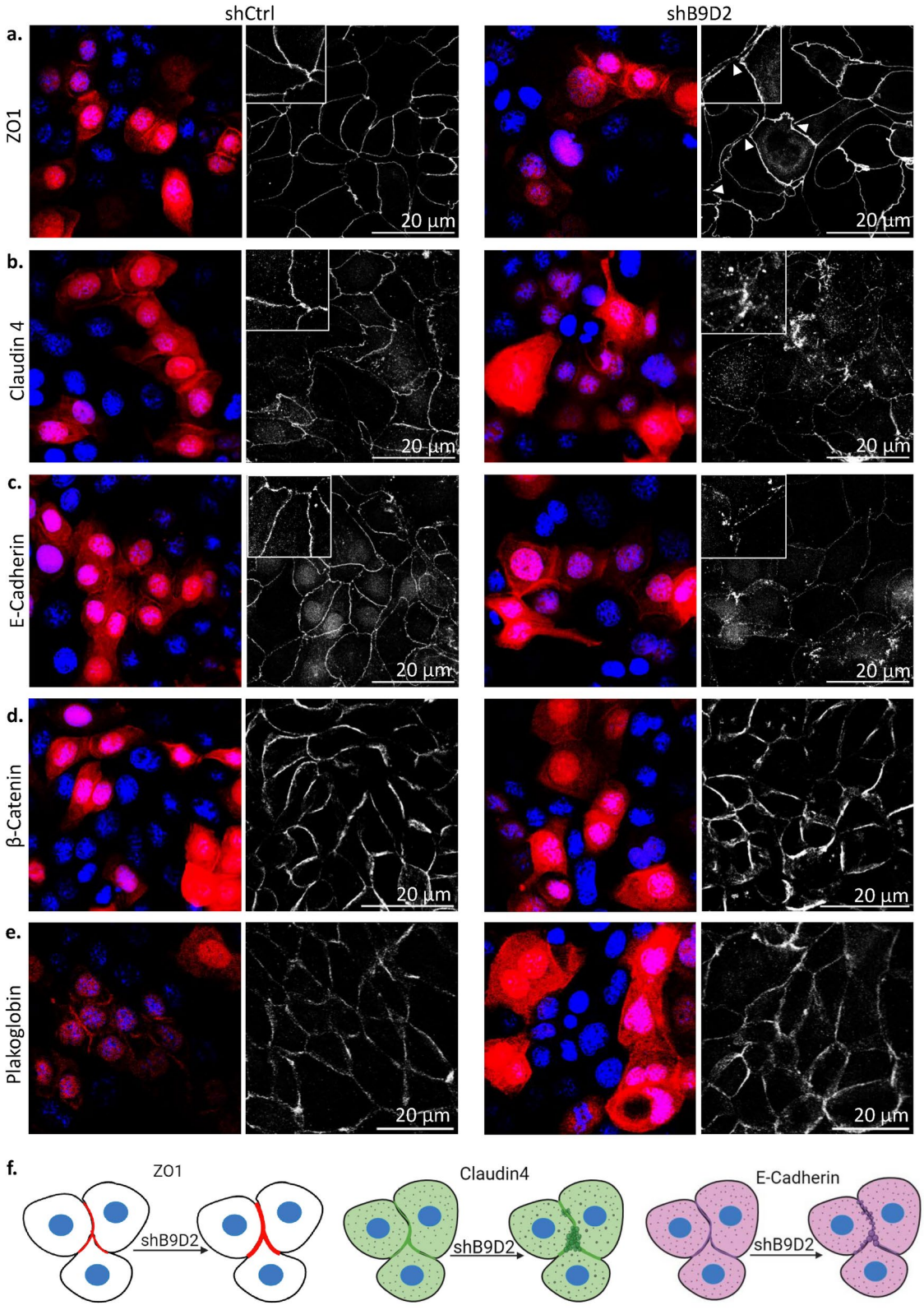

Fig. 4. Role of B9D2 in tight junction proteins localization. Immunostaining of junction proteins in NRC epithelial cells after transfection with sh-Ctrl-RFP or sh-B9D2-3-RFP. Transfected cells are labelled in red. Confocal projection of (**a**) ZO1, Arrowheads designate the interruptions in ZO1 labeling. (**b**)/ Claudin 4, (**c**)/ E-cadherin, (**d**)/ β-catenin and Confocal focal plane of (**e**)/ Plakoglobin. The square in the upper left part of the images shows a magnification of the immune labeling of the junctions. (**f**)/ Schematic diagram of B9D2 knockdown-induced redistribution of junction proteins.

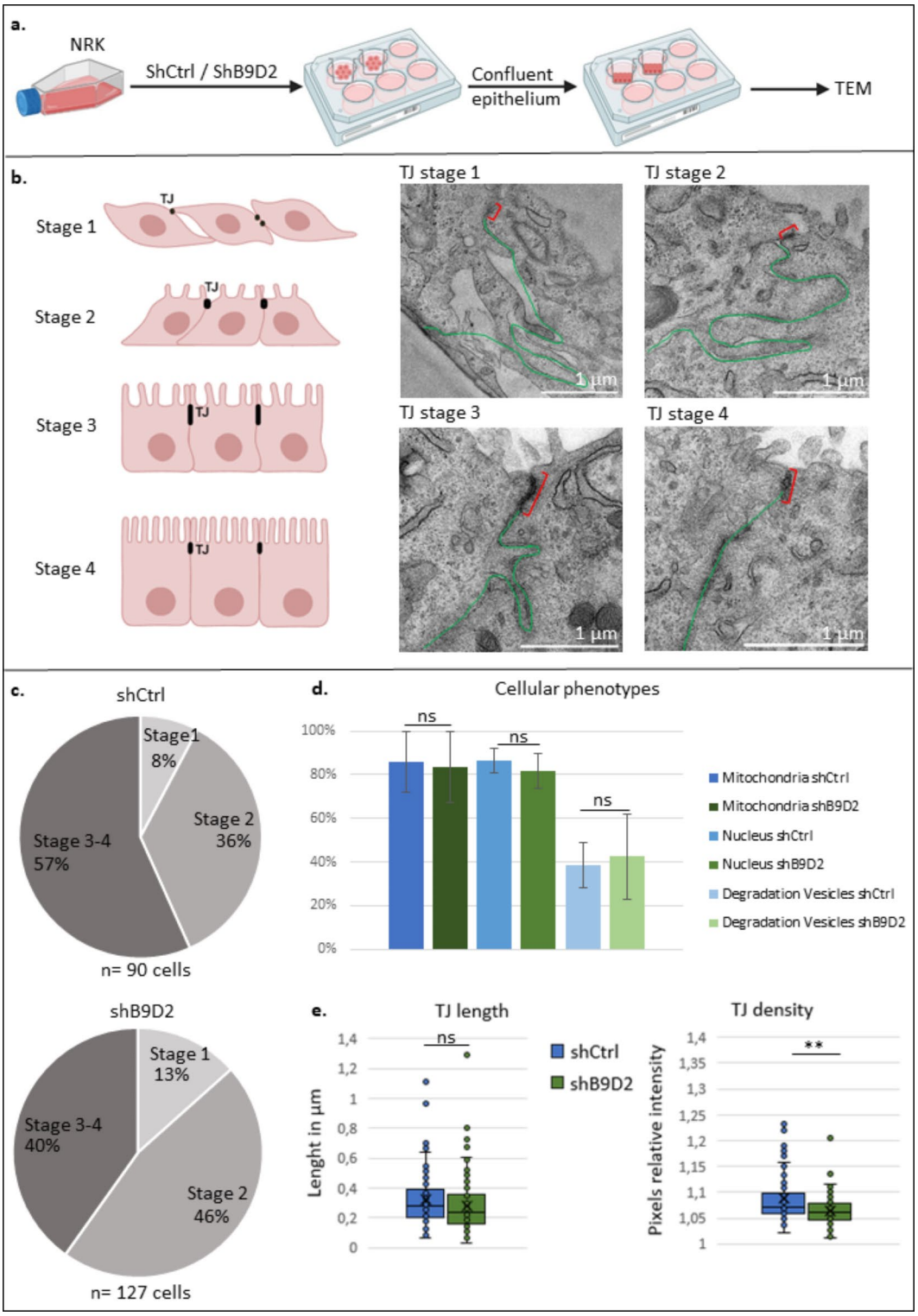

Fig. 5. B9D2 function in structural maintenance of tight junctions. (**a**)/ Flow chart of the experiment (**b**)/ Diagram displaying the major stages of tight junctions maturation during epithelial polarization and corresponding TEM images in NRK epithelia. Green lines outline cell membranes and red brackets highlight tight junctions (= TJ). (**c**)/ Percentage of shControl versus shB9D2-3 transfected cells, classified according to categories defined in b. Khi-deux test : pvalue = $8{,}9^{E}$-09. N = 2 ind. (**d**)/ Analysis of structural characteristics in (shCtrl) or (shB9D2-3) transfected cells. The diagram shows the percentage + /- Min–Max of unaltered over altered organelles, namely: morphology of mitochondria and nuclei as well as the presence of degradation (multilamellar) vesicles. Khi-deux test. (**e**)/ Quantification of tight junctions' length and density ratio (TJ/cytosol) over the whole cell's pannel. Student Test type 3, pvalue < 0,01.

of the cells attested by less membrane curvatures. Stage 4 corresponds to the mature TJ, less extended, with a straight membrane, characteristic of fully polarized cells. The classification of the observed cells into the 4 stages described previously (Fig. 5C) revealed that B9D2 knockdown led to the reduction of the category "polarized" stage 3–4 (57% of shCtrl cells against 40% of shB9D2 cells) and an increase of the group of stage 1–2 (44% of shCtrl cells against 59% of shB9D2 cells) suggesting that B9D2 is involved in TJ maturation. Moreover, a careful examination of the ultrastructure of the shCtrl versus shB9D2 transfected cells did not detect any significant effect on nuclear or mitochondrial morphologies nor on the presence or number of degradation vesicles (Fig. 5D), suggesting that B9D2 knockdown affects specifically the TJ. Finally, the analysis of the TJ structural characteristics made over the full cell sample (Fig. 5E) confirmed a global reduction of the TJ density, without significant modification of their length, reinforcing the conclusion that the role of B9D2 in TJ structure impacts cell junction maturation and epithelial polarity.

B9D2 is necessary for cell junctions' tightness

Given the role of B9D2 in the structure of TJ, we wanted to check whether its expression could affect the sealing properties of the epithelium.

After transfection with shCtrl or shB9D2, NRCs were cultured on inserts until confluence (Fig. 6A). After 7 days, the measurement conditions were controlled, i.e., the fully confluent nature of the epithelia and a transfection rate of at least 50% (Fig. 6B). Trans-Epithelial Resistance (TER) was then measured every hour during about 4 to 5 days. Figure 6C displays the results of a representative experiment where TER of Ctrl- or shB9D2-transfected NRC confluent monolayers were measured over 103h. One can see in the shCtrl epithelium, the regular increase of the TER value until more than 4000 ohms.cm^2 during the first 30h corresponding to the physiological maturation of the TJ, followed by a slow decrease that reflects the degradation of the epithelium caused by the inevitable cellular death in these culture conditions. Contrasting with this situation, the kinetics of the NRC epithelia transfected with shB9D2-1, shB9D2-2 or shB9D2-3 do not display any progression with values constantly low throughout the duration of the monitoring. The distributions of TER values of 5 (Ctrl cells) or 9 (shB9D2 cells) independent experiments measured over 3 days (D8 to D10) are depicted in Fig. 6D. It appears that whereas the average TER values reach a maximum of about 2000 ohms.cm^2 (Ctrl NRC) or 2500 ohms.cm^2 (shCtrl NRC), the epithelium transfected with each of the three different shB9D2 remain with average TER values that do not exceed 500 ohms.cm^2.

These results demonstrate that B9D2 expression is necessary for the tight junction sealing function.

B9D2 knockdown impairs cysts lumenogenesis

Finally, with the aim to understand the implications of B9D2 dysfunction in the context of biliary duct malformations observed in MKS and Joubert ciliopathies, we investigated its role in biliary epithelial morphogenesis in 3D culture[25]. When grown in a suitable extracellular matrix, epithelial cells self-organize into hollow spheres called cysts, which consist in a monolayer of epithelial cells surrounding a central lumen. This process requires the establishment of the epithelial apico-basal polarity and cell junctions, that will participate in the extension of the central lumen through the secretion of solutes and water by the apical transporters and the retention by the TJ barrier[26].

We have previously shown that NRCs develop into cysts when cultured in 3D Matrigel[25]. In this experiment, cells transfected with shCtrl or two different shB9D2s (shB9D2-1 and shB9D2-3) were mixed with Matrigel and cultured for 5 days until optimal cyst formation (Fig. 7A). The quantitative analysis was carried out selectively on RFP expressing cysts (Fig. 7B) and involved: (i) the percentage of cysts, i.e., the number of correctly formed cysts (rounded cyst with a single lumen) over multiluminal cysts / oval cysts / spheroids / random structures (Fig. 7C) and (ii) the cyst diameters which were measured and plotted using ImageJ software (Fig. 7D). While B9D2 depletion did not significantly affect the efficacy of cyst formation, it led to a significant reduction of cyst diameters.

To further evaluate the function of B9D2 in lumen growth, we tested cholangiocyte secretion function under Ctrl versus B9D2 knockdown conditions, using fluorescein diacetate (FDA) secretion test (see Materials and Methods). The FDA hydrolysed to fluorescein by nonspecific intracellular esterases after cellular uptake will be secreted into the lumen in actively secreting cysts through transport by apical MRP2 transporter. Figure 7E depicts green fluorescent images of Ctrl or shB9D2 transfected cysts where non secreting cysts appear as a ring of fluorescent cells (which have retained fluorescein) contrasting with secretory cysts in which fluorescein has been secreted into the lumen. The comparative analysis of the relative luminal fluorescence (luminal fluorescence divided by the cyst area) of Ctrl NRC cysts or RFP positive shCtrl or shB9D2 NRC cysts (over respectively 123 Ctrl and 62 B9D2 knockdown cysts) did not detect any difference in secretory activity between Ctrl and B9D2 knockdown cysts (Fig. 7F).

Altogether, these observations suggest that B9D2 is not essential for cyst formation nor for secretory activity, but its expression is necessary to allow lumen extension by ensuring the epithelial tightness.

Interaction of B9D2 with lipids

We finally explored the possible interaction of B9D2 with specific membrane lipids. Thus, B9D2 is almost restricted to its functional B9 domain which belongs to the class of lipid binding C2 domains[11,27]. While most of C2 domain were shown to interact with negatively charged phospholipids by virtue of their positive and hydrophobic residue β-sheet surface, some were shown to feature interactions with phosphoinositides[28]. We then probed the interaction of B9D2 with phospholipids and phosphoinositides by incubating corresponding lipid membrane strips with total protein extracts from B9D2-eGFP versus eGFP overexpressing HEK cells. Figure 8 which corresponds to the image of the blot probed with an anti-GFP antibody reveals a strong binding of B9D2 to PI4P, PI(3,4,5)P3 and to a lesser extent PI(4,5)P2.

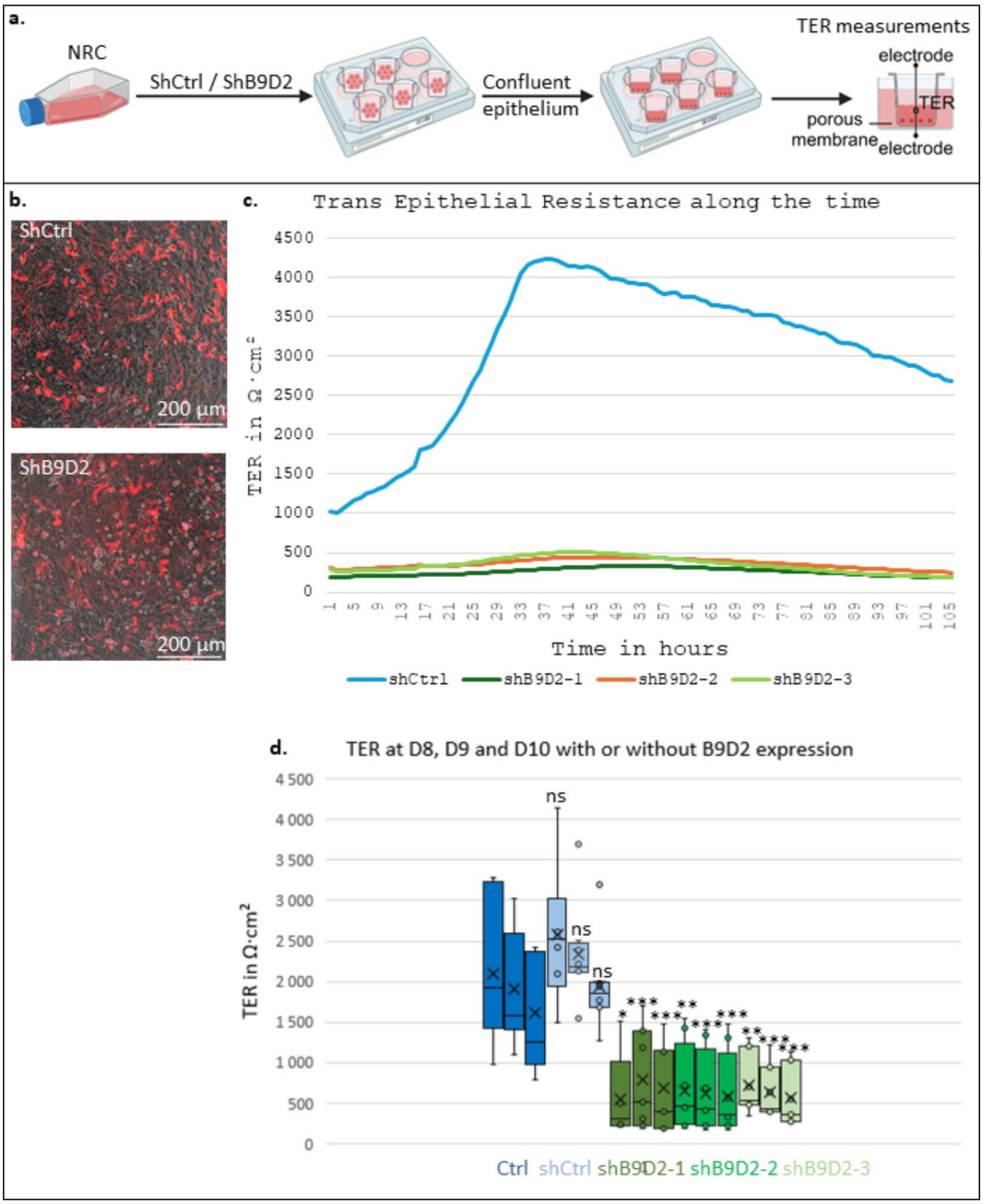

Fig.6. B9D2 function in epithelial tightness. (**a**)/ Diagram of the experimental procedure (**b**)/ Images of NRC epithelium before measurements ; red cells are expressing RFP-shRNA (CTRL or B9D2). (**c**)/ Representative graph of Trans-Epithelial Resistance (TER ; in ohms.cm^2) in confluent Ctrl or shB9D2 NRC epithelia during the establishment of epithelial polarity. Measurements were made every hour during 4 days on NRC monolayers transfected either with shRNACtrl or one of the 3 shRNAs targeted against B9D2 (B9D2-1, B9D2-2 and B9D2-3) and cultured with serum. (**d**)/ Distribution of TER measurements in confluent NRC epithelia respectively: untransfected (Ctrl) or transfected with shRNA Ctrl or one of the 3 shRNAs. Mann–Whitney statistic test : shCtrl compared to Ctrl; shB9D2 compared to shCtrl. *** pvalue < 0,001 **pvalue < 0,005 *pvalue < 0,01. N = 5–9.

Discussion

In this work, we revealed that the B9D2 protein, besides its localization to the transition zone of the primary cilium, performs additional extraciliary functions in epithelium formation and maintenance.

Like other ciliary proteins of the transition zone, in particular several proteins of the NPHP module, which are also found at cell junctions or at the nucleus[23,24,29], B9D2 was found at the tight junctions in polarized epithelia and partially at the nucleus in non-polarized cells. This dual location at nuclear and junctional membranes raises the question of the interaction of B9D2 with compartmentalized lipid domains. The specific interaction revealed

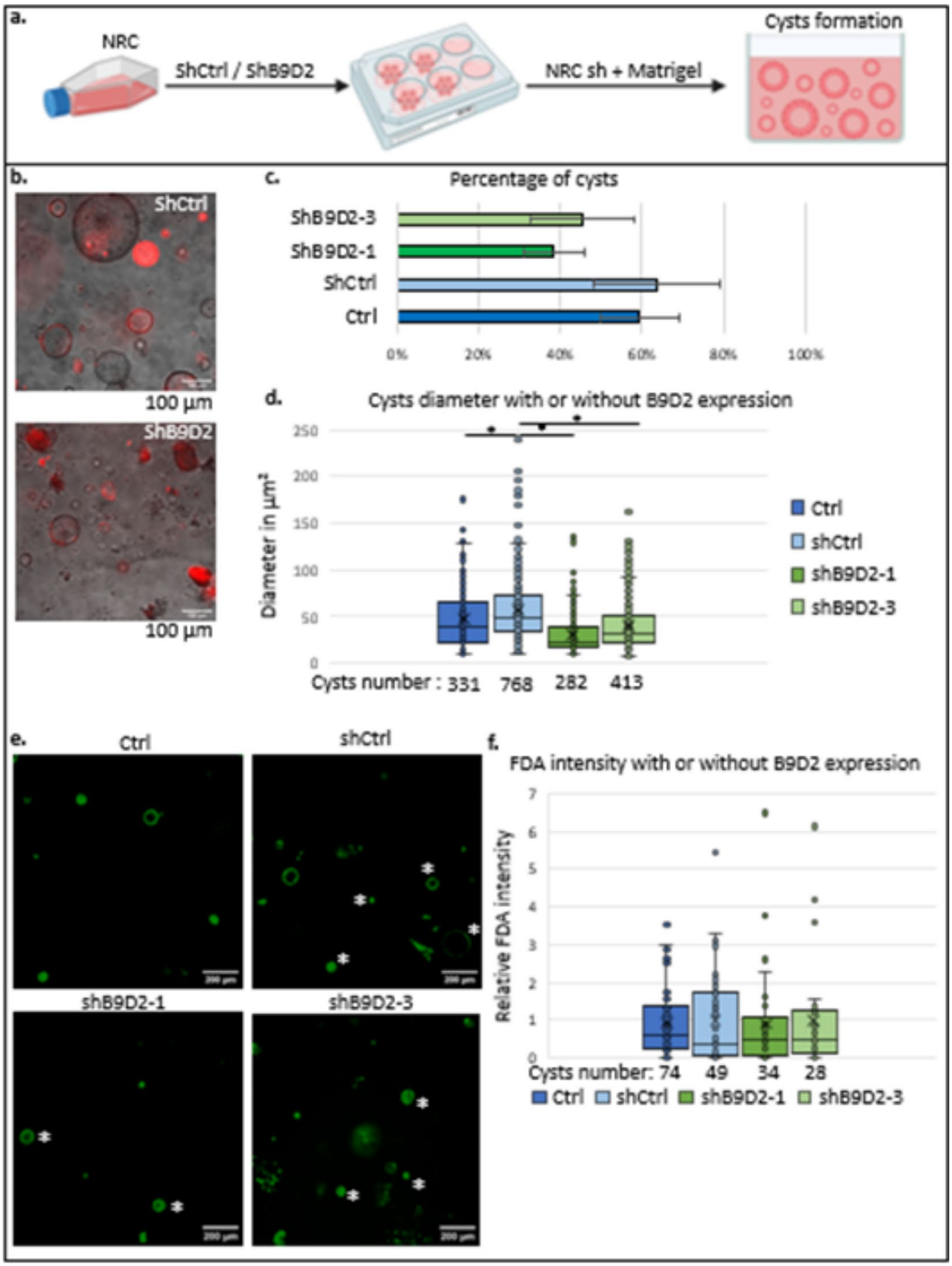

Fig. 7. B9D2 function in lumenogenesis. (**a**)/ Experimental flow chart. (**b**)/ Images of cysts after NRCs transfection with shCtrl or shB9D2 fused to RFP. ShRNA expressing cells appear in red. (**c**)/ Percentage + /- SD at day5 of regular cysts over abnormal cysts + non cystic 3D structures. Khi-deux test. pvalue = ns. N = 4. (**d**)/ Measurements of cysts diameter in the same samples. Student test type 3 : shCtrl compared to Ctrl ; shB9D2 compared to shCtrl. * pvalue < 0,01. N = 4. (**e**)/Fluorescence images of NRC cysts cultured in Matrigel, taken 5 min after FDA treatment, at peak intensity of the green fluorescein secretion in the lumen. Transfected sh-cysts were marked by an asterisk. (**f**)/ Quantification of the ratio FDA intensity over cyst area. Only sh RNA expressing cysts (RFP positive) were considered for the secretion measurements. Student test type 3 or test Z for shB9D2-3, N = 2. Ctrl compared to shCtrl, shCtrl compared to shB9D2. pvalue = ns.

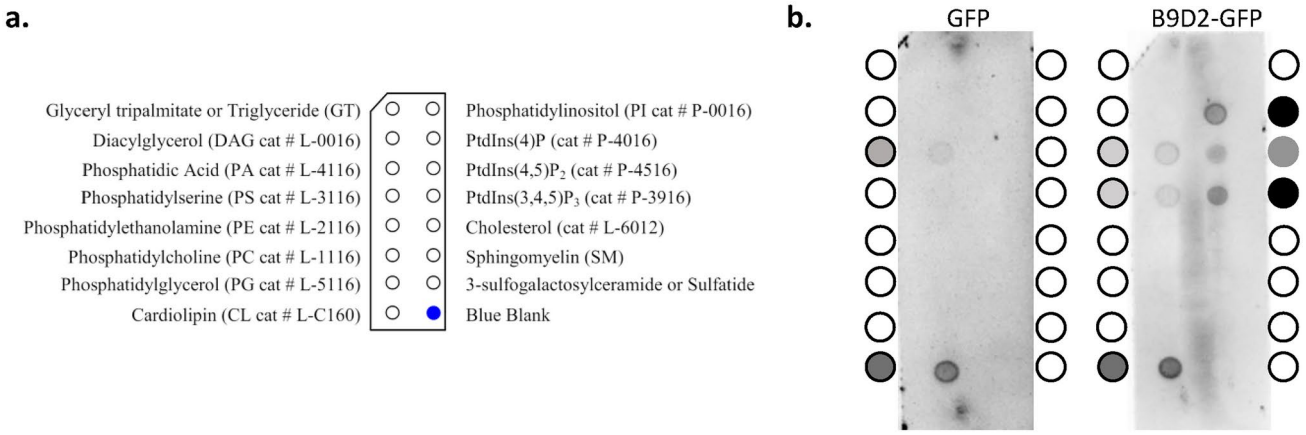

Fig. 8. B9 domain interacts with phosphoinositides. (**a**)/ Identification of lipid membrane strips (from manufacturer datasheet). (**b**)/ HEK cells were transfected with pGFP or pB9D2-GFP during 48h. Cells extracts were collected and a concentration of 1.5 mg/mL of total proteins was incubated on lipid membrane strips. The interaction between GFP or B9D2-GFP with lipids was immunorevealed with a GFP antibody.

in this work with some phosphoinositides might explain why B9D2 is found in specific regions such as TJ, nuclear membrane or ciliary transition zone where PI4P, PI(3,4,5)P3 and PI(4,5)P2 are involved in neighboring membrane patches compartmentalization[30–33].

This interaction of the B9 domain with lipids fits with previous works where super resolution imaging could localize B9 domain proteins near the ciliary membrane at the transition zone[34–36]. However, although it has been shown that B9D2 expression is essential to the construction of the multiproteic complexes of the transition zone, and to the ciliary localization of transmembrane or lipidated ciliary proteins, no definitive hypothesis regarding the role of B9 domain in protein–protein or protein-lipid interactions has yet emerged[12]. Here, we show that before ciliogenesis, B9D2 localizes to the TJ, close to cell membrane and to zonula occludens protein ZO1. B9D2 deficiency leads to mislocalization of ZO1, as well as junctional transmembrane proteins Claudin 4 and E cadherin. Interestingly, in B9D2 knockdown cells, the ZO1 protein revealed by immunostaining appears extended ectopically into the cytosol along the membrane compared to the continuous and thin belt it forms around the control cells. This is reminiscent of phenotypes displayed by cells carrying ZO1 mutations that prevent the formation of the junctional plaque by inhibiting the preliminary phase transition of ZO proteins (ZO1 and ZO2) into high ordered oligomers[37,38]. Much like in these mutants, where the lack of a condensed ZO proteins domain was shown to inhibit the sequestration of key TJ proteins, we noticed that B9D2 knockdown prevented the incorporation of Claudin 4 at the junctional plaque with subsequent loss of epithelium tightness and maturation. Our hypothesis is that at the TJ, through the interaction of its B9 domain with phosphoinositides domains at the limit between apical and basal epithelial membranes, B9D2 contributes to the clustering of ZO proteins near the membrane. This assumption of a scaffolding role of B9D2 for the formation and stabilisation of membrane-linked multiprotein complexes holds true also for the transition zone which is only partly abolished in B9D2 knock out conditions.

Finally, our main question was how this new function of B9D2 in TJ could account for the tubulogenesis defects present in the liver, which characterize ciliopathies induced by B9D2 mutations. Biliary tubulogenesis requires the formation and expansion of lumens from polarized cholangiocytic epithelia. Luminal formation initiates within the 2D epithelium through cell interactions with the extracellular matrix and between neighboring cells. This information guides cellular polarization, marked by the asymmetric localization of apico-basal polarity complexes and the establishment of the apical membrane initiation site (AMIS). Regulation of this lumen formation process involves a network of polarity proteins, the cytoskeleton and a polarized vesicular traffic. Once the lumen is established, it expands via fluid secretion facilitated by the paracellular permeability of TJ proteins present at the matured AMIS, now termed the pre-apical patch (PAP), and by pumps and ion channels[26,39]. In our study, B9D2 does not influence cyst formation nor secretion via apical transporters, indicating that the cells are sufficiently polarized to initiate lumen formation. However, B9D2 knockdown cells form cysts whose average diameter is half that of control cysts. This suggests that B9D2 is not necessary for the initial stages of lumen formation dependent on apico-basal polarity and apical actin constriction; insofar as cysts are not composed solely of transfected cells, it cannot be ruled out that residual B9D2 expression may collectively compensate for B9D2 deficiency. In contrast, B9D2's role in maintaining TJ is crucial for lumen extension. The restricted extension of the lumen of B9D2 knockdown cysts can be attributed to the increased permeability of TJ, leading to leakage of the secreted lumen. These defects in lumen extension could in part account for the morphogenetic abnormalities of the bile ducts observed in MKS and Joubert ciliopathies.

This work provides new avenues for understanding abnormalities in biliary tubulogenesis, which could extend to the renal tubular system, which also shows abnormalities in morphogenesis in TZ protein-related ciliopathies[29]. More broadly, exploring the extraciliary functions of these proteins could contribute to a better understanding of the complex clinical pictures of ciliopathies.

Materials and methods

Cell culture

NRC cells (Normal Rat Cholangiocytes, from Prof. Larusso) are cultured as described in Vroman and Larusso[40] and Bouzhir, et al.[25]. NRK (Normal Rat Kidney, NRK 52E), used for the high sh-transfection rate around 80% (Supplementary Fig. S2C), and HEK-293 (Human Embryonic Kidney, CRL-1573 ATCC) cells were cultured in DMEM Glutamax (61965, Gibco), 10% SVF and 1% PSF. All cells were maintained in a humid atmosphere at 37°C, 5% CO2. In this study, both cell lines (NRC and NRK) were maintained in culture with serum until 5 days (NRC) or 3 days (NRK) after confluency, in order to keep the amount of ciliated cells below 5%. In any case, serum starvation at confluency in the same culture conditions led to only 17% ciliated cells (Supplementary Fig. S1).

Immunofluorescence

NRC cells are seeded onto collagen-coated LabTek Permanox (NUNC ref 177445) or coverslips (12 mm, No. 1.5H) for SIM experiments, and NRK cells onto glass LabTek (NUNC ref 154534). The confluent epithelium is fixed in 2% formaldehyde 15 min followed by permeabilization in 1% Triton X-100 10 min, at room temperature (RT). Between each step, 3 washes of 5 min were performed with 1X PBS. Non-specific antigen interactions were blocked with 1% BSA-10% Goat serum in 1X PBS for 1 h at RT. Primary antibodies, diluted at 1:100, were incubated for 2 h at RT or overnight at 4°C and secondary antibodies diluted at 1:500 for 1 h at RT protected from light. The slide was mounted with mounting medium containing DAPI (Ref Sigma F6057-20ML). Antibodies: B9D2 Sigma (HPA042229) ; Acetylated-Tubulin Sigma (T7451) ; β-Catenin BD Biosciences (610154) ; Claudin4 Invitrogen (329400) ; E-Cadherin Invitrogen (13190) ; Plakoglobin = γ-Catenin Invitrogen (138500) ; ZO1 Invitrogen (339100) ; ZO2 BD Transduction (611560).

shRNA

The shRNAs were purchased from Dharmacon (USA). For B9D2 knockdown, 3 shRNAs were tested (see Table 1). NRCs and NRKs were transfected with lentiviruses containing shB9D2 at MOI = 1 and 8 µg/mL of polybrene transfectant (TR-1003-G EMD Millipore Corporation) in DMEM-F12 medium for NRCs and DMEM-High Glucose (SH300081.02, Cytiva) for NRKs during 20 h. Then the medium was replaced by complete culture medium. At Day7, the cells were recovered to verify silencing efficiency by immunoblots (see Supplementary Fig. S2A & S2B) or subcultured for phenotypic analysis. Most phenotypic analyses were carried out between Day7 and Day11 and the phenotypes of shB9D2 cells were compared with cells transfected with shCtrl (scramble shRNA, Dharmacon).

Protein extraction and blot analysis

Cells were rinsed with 1X PBS, then lysed in RIPA buffer (25 mM Tris–HCl pH 7.6, 150 mM NaCl, 1% NP-40, 0.1% SDS, 1% Na-Deoxycholate, 1 mM PMSF, 1 anti-proteases tablet / 10 mL (11,836,170,001, Roche)) and centrifuged at 13.300 g for 15 min at 4 ℃. The proteins were quantified using the BCA Protein Assay Kit (Thermo Fisher Scientific). For Western Blots, proteins were separated on SDS-PAGE gel at constant voltage for 1 h – 2 h. Then transferred to nitrocellulose membranes (10,600,008, Cytiva) at 5 mA/cm2 of membrane for 30 min. Membranes were incubated with ponceau red for 10 min to check transfer, then rinsed 3 times in distilled water. Membranes were incubated for 1 h in blocking solution (5% skimmed milk in 1X PBS-Tween) and then with primary antibodies, diluted at 1:1000 (B9D2) or 1:4000 (β-actine, ref Sigma A1978), overnight at 4 ℃ and finally for 1 h with secondary antibodies, diluted at 1:2000, at RT. For Lipid Strip Assay, membranes (Echelon Biosciences P6002) were incubated for 1h30 with a 1% skimmed milk before addition of 1.5 mg total protein extract from HEK cells transfected by pEGFP (6085–1, Clontech Laboratories) or pB9D2-GFP (ORa03720C, Genscript) plasmids, following the Mirus TransIT-X2 protocol, for 1 h. Then incubated with primary antibodies (anti-GFP, dilution 1:1000, ref Roche 118144) overnight at 4 ℃ and with secondary antibodies 1 h at RT. Membranes are revealed using the Bio-Rad chemiluminescence kit (170–5061, Clarity Western ECL Substrate). Images were taken using the Spectra Fusion FX7 system (Vilber Lourmat). Quantification and blot analysis were performed using ImageJ software.

TER measurements

TER (Transepithelial electrical resistance) is measured using the CellZscope (NanoAnalytics). An electrode on each side of the cell layer is used to measure its resistance. In these experiments, NRCs cells are seeded in 0.9 cm^2 inserts (Falcon 353180) coated with collagen I. At confluence, the inserts are placed in the CellZscope and TER measurements done every 1 h during 3–5 days.

shRNA	Product references	Sequence
shCtrl	SMARTvector non-targeting negative control hEF1α-TurboRFP-NTC	–
shB9D2-1	pSMART hEF1α-TurboRFP / V3SR7594-237,896,925	5′ AGCTAGCACGGGCTTTCGT 3′
shB9D2-2	pSMART hEF1α-TurboRFP / V3SR7594-240,506,531	5′ ACGGGTTTCTCTGAAGGTA 3′
shB9D2-3	pSMART hEF1α-TurboRFP / V3SR7594-243,762,117	5′ CACTGTCAGGGGCACTTAA 3′

Table 1. shRNAs sequences.

Transmission electronic microscopy

Cells inclusion

NRK cells were seeded in 0.9 cm^2 inserts (353,180, Falcon). At confluence, the cells were fixed with 2.5% Glutaraldehyde diluted in 0.1 M cacodylate buffer for 1h15 at RT and stored overnight at 4 ℃ in fixative solution. Cells were rinsed 5 times for 5 min with 0.1 M cacodylate buffer. Samples were postfixed with 1% Osmium-1.5% Potassium Ferrocyanide solution 1 h at RT under agitation. Cells were rinsed 3 times 5 min with water. Cells were dehydrated in graded ethanol series, under agitation: 15 min ethanol 50%, 15 min ethanol 70%, 20 min ethanol 80% and 3 × 15 min ethanol 90%. Once dehydrated, the cells were progressively impregnated with HPMA and EPON resin: 20 min HPMA 90%-Ethanol90 10%, 20 min HPMA 95%-Ethanol90 5%, 20 min HPMA 97%-Ethanol90 3%, 1h30 HPMA 2/3-Epon1/3, 1h30 HPMA1/2-Epon1/2. Samples were covered by Epon overnight at RT. Then, the bottom of inserts, containing the cells, was cut into strips. The strips were placed on sandwich in a mould containing Epon, placed in an oven at 60 ℃ for 24 h to polymerize.

Cells preparation for ultrastructural study

Ultrathin sections (80 nm) were cut with an ultramicrotome EM UC6 (Leica Microsystems), collected on formvar carbon-coated copper grids and stained in 2% uranyl acetate (Merck) and lead citrate before observation. Grids were examined under a JEM 1400 TEM operating at 80 kV (JEOL). TEM Images were acquired using a post-column high-resolution (9 megapixels) high-speed camera (RIO9; Gatan) and processed with Digital Micrograph (Gatan) and ImageJ software.

Cysts formation

Cysts were generated from NRCs following our published protocol[25]. FDA assays were performed as described in Bouzhir et al.[25]. For the analysis, only RFP expressing cysts with shCtrl or shB9D2 were considered. Cysts size analysis was performed by measuring cysts diameter using ImageJ software. Quantification of the percentage of cysts corresponds to the number of cysts on the total number of multicellular structures (cysts + other structures).

Microscopy image acquisition and analysis

For immunofluorescence experiments, the images were taken on the confocal microscope (Zeiss LSM 700) with a Plan APO 60X/1.4 immersion oil objective (Nikon) with 518F immersion oil (Zeiss). All images were processed using ImageJ and NIS element softwares.

For Structured illumination microscopy (SIM), experiments were performed on a ZEISS Elyra 7 – Lattice SIM equipped with a 63 × Plan-Apochromat (N.A. 1.4) oil immersion objective and coupled with a PCO.edge sCMOS camera (pixel size: 6.5 µm; bit depth 16 bit). For both channels, 13 phases of 250 ms each were used for each plane and an optimized z-step of 110 nm was used to generate 3D-SIM acquisitions. SIM processing was performed on ZEN Black (ZEISS, version 16.0) and to correct chromatic aberrations, alignment procedure (ZEN Black) was applied on both channels after measurements on multispectral calibration beads.

Cysts were imaged at Day5, with Plan Fluor 10X/0.30 objective, on the inverted fluorescence microscope (Nikon Eclipse TE2000 with a Hamamatsu CMOS camera) and were analyzed using ImageJ software.

Data availability

All data generated and/or analyzed during this study are included in this published article (and its Supplementary Information files).

Received: 9 July 2024; Accepted: 7 October 2024
Published online: 25 October 2024

References

1. Dowdle, W. E. et al. Disruption of a ciliary B9 protein complex causes Meckel syndrome. *Am. J. Hum. Genet.* **89**, 94–110. https://doi.org/10.1016/j.ajhg.2011.06.003 (2011).
2. Radhakrishnan, P., Nayak, S. S., Shukla, A., Lindstrand, A. & Girisha, K. M. Meckel syndrome: Clinical and mutation profile in six fetuses. *Clin. Genet.* **96**, 560–565. https://doi.org/10.1111/cge.13623 (2019).
3. Bachmann-Gagescu, R. et al. Joubert syndrome: a model for untangling recessive disorders with extreme genetic heterogeneity. *J. Med. Genet.* **52**, 514–522. https://doi.org/10.1136/jmedgenet-2015-103087 (2015).
4. Dallali, H. et al. Multiallelic rare variants in BBS genes support an oligogenic ciliopathy in a non-obese juvenile-onset syndromic diabetic patient: a case report. *Front. Genet.* **12**, 664963. https://doi.org/10.3389/fgene.2021.664963 (2021).
5. Satir, P. & Christensen, S. T. Overview of structure and function of mammalian cilia. *Annu. Rev. Physiol.* **69**, 377–400. https://doi.org/10.1146/annurev.physiol.69.040705.141236 (2007).
6. Basten, S. G. & Giles, R. H. Functional aspects of primary cilia in signaling, cell cycle and tumorigenesis. *Cilia* **2**, 6. https://doi.org/10.1186/2046-2530-2-6 (2013).
7. Hartill, V., Szymanska, K., Sharif, S. M., Wheway, G. & Johnson, C. A. Meckel-Gruber syndrome: an update on diagnosis, clinical management, and research advances. *Front. Pediatr.* **5**, 244. https://doi.org/10.3389/fped.2017.00244 (2017).
8. Gana, S., Serpieri, V. & Valente, E. M. Genotype-phenotype correlates in Joubert syndrome: A review. *Am. J. Med. Genet. C Semin Med. Genet* **190**, 72–88. https://doi.org/10.1002/ajmg.c.31963 (2022).
9. Lemaigre, F. P. Mechanisms of liver development: concepts for understanding liver disorders and design of novel therapies. *Gastroenterology* **137**, 62–79. https://doi.org/10.1053/j.gastro.2009.03.035 (2009).
10. Fabris, L. et al. Pathobiology of inherited biliary diseases: a roadmap to understand acquired liver diseases. *Nat. Rev. Gastroenterol. Hepatol.* **16**, 497–511. https://doi.org/10.1038/s41575-019-0156-4 (2019).
11. Zhang, D. & Aravind, L. Identification of novel families and classification of the C2 domain superfamily elucidate the origin and evolution of membrane targeting activities in eukaryotes. *Gene* **469**, 18–30. https://doi.org/10.1016/j.gene.2010.08.006 (2010).
12. Okazaki, M. et al. Formation of the B9-domain protein complex MKS1-B9D2-B9D1 is essential as a diffusion barrier for ciliary membrane proteins. *Mol. Biol. Cell* **31**, 2259–2268. https://doi.org/10.1091/mbc.E20-03-0208 (2020).

13. Dawe, H. R. et al. The Meckel-Gruber syndrome proteins MKS1 and meckelin interact and are required for primary cilium formation. *Hum. Mol. Genet.* **16**, 173–186. https://doi.org/10.1093/hmg/ddl459 (2007).
14. Williams, C. L., Winkelbauer, M. E., Schafer, J. C., Michaud, E. J. & Yoder, B. K. Functional redundancy of the B9 proteins and nephrocystins in Caenorhabditis elegans ciliogenesis. *Mol. Biol. Cell* **19**, 2154–2168. https://doi.org/10.1091/mbc.e07-10-1070 (2008).
15. Zhao, C. & Malicki, J. Nephrocystins and MKS proteins interact with IFT particle and facilitate transport of selected ciliary cargos. *EMBO J.* **30**, 2532–2544. https://doi.org/10.1038/emboj.2011.165 (2011).
16. Cui, C. et al. Disruption of Mks1 localization to the mother centriole causes cilia defects and developmental malformations in Meckel-Gruber syndrome. *Dis. Model Mech.* **4**, 43–56. https://doi.org/10.1242/dmm.006262 (2011).
17. Wheway, G. et al. Aberrant Wnt signalling and cellular over-proliferation in a novel mouse model of Meckel-Gruber syndrome. *Dev. Biol.* **377**, 55–66. https://doi.org/10.1016/j.ydbio.2013.02.015 (2013).
18. Town, T. et al. The stumpy gene is required for mammalian ciliogenesis. *Proc. Natl. Acad. Sci. U. S. A.* **105**, 2853–2858. https://doi.org/10.1073/pnas.0712385105 (2008).
19. Wang, J. et al. Variable phenotypes and penetrance between and within different zebrafish ciliary transition zone mutants. *Dis. Model Mech.*https://doi.org/10.1242/dmm.049568 (2022).
20. Strazzabosco, M. & Fabris, L. Development of the bile ducts: essentials for the clinical hepatologist. *J. Hepatol.* **56**, 1159–1170. https://doi.org/10.1016/j.jhep.2011.09.022 (2012).
21. Hua, K. & Ferland, R. J. Primary cilia proteins: ciliary and extraciliary sites and functions. *Cell Mol. Life Sci.* **75**, 1521–1540. https://doi.org/10.1007/s00018-017-2740-5 (2018).
22. Nurnberger, J., Bacallao, R. L. & Phillips, C. L. Inversin forms a complex with catenins and N-cadherin in polarized epithelial cells. *Mol. Biol. Cell* **13**, 3096–3106. https://doi.org/10.1091/mbc.e02-04-0195 (2002).
23. Delous, M. et al. Nephrocystin-1 and nephrocystin-4 are required for epithelial morphogenesis and associate with PALS1/PATJ and Par6. *Hum. Mol. Genet.* **18**, 4711–4723. https://doi.org/10.1093/hmg/ddp434 (2009).
24. Wolf, M. T. & Hildebrandt, F. Nephronophthisis. *Pediatr. Nephrol.* **26**, 181–194. https://doi.org/10.1007/s00467-010-1585-z (2011).
25. Bouzhir, L., Gontran, E., Loarca, L., Collado-Hilly, M. & Dupuis-Williams, P. Generation and quantitative characterization of functional and polarized biliary epithelial cysts. *J. Vis. Exp.*https://doi.org/10.3791/61404 (2020).
26. Datta, A., Bryant, D. M. & Mostov, K. E. Molecular regulation of lumen morphogenesis. *Curr. Biol.* **21**, R126-136. https://doi.org/10.1016/j.cub.2010.12.003 (2011).
27. Corbalan-Garcia, S. & Gomez-Fernandez, J. C. Signaling through C2 domains: more than one lipid target. *Biochim. Biophys. Acta* **1838**, 1536–1547. https://doi.org/10.1016/j.bbamem.2014.01.008 (2014).
28. Joshi, A. S., Ragusa, J. V., Prinz, W. A. & Cohen, S. Multiple C2 domain-containing transmembrane proteins promote lipid droplet biogenesis and growth at specialized endoplasmic reticulum subdomains. *Mol. Biol. Cell* **32**, 1147–1157. https://doi.org/10.1091/mbc.E20-09-0590 (2021).
29. Srivastava, S., Molinari, E., Raman, S. & Sayer, J. A. Many genes-one disease? genetics of Nephronophthisis (NPHP) and NPHP-associated disorders. *Front. Pediatr.* **5**, 287. https://doi.org/10.3389/fped.2017.00287 (2017).
30. Chen, C., Hu, J. & Ling, K. The role of primary cilia-associated phosphoinositide signaling in development. *J. Dev. Biol.*https://doi.org/10.3390/jdb10040051 (2022).
31. Shewan, A., Eastburn, D. J. & Mostov, K. Phosphoinositides in cell architecture. *Cold Spring Harb. Perspect. Biol.* **3**, a004796. https://doi.org/10.1101/cshperspect.a004796 (2011).
32. Van, I. S. C. D., Agnetti, J. & Gassama-Diagne, A. Mechanisms behind the polarized distribution of lipids in epithelial cells. *Biochim. Biophys. Acta. Biomembr.* **1862**, 183145. https://doi.org/10.1016/j.bbamem.2019.183145 (2020).
33. Fiume, R. et al. Nuclear phosphoinositides: their regulation and roles in nuclear functions. *Int. J. Mol. Sci.*https://doi.org/10.3390/ijms20122991 (2019).
34. Yang, T. T. et al. Superresolution pattern recognition reveals the architectural map of the ciliary transition zone. *Sci. Rep.* **5**, 14096. https://doi.org/10.1038/srep14096 (2015).
35. Shi, X. et al. Super-resolution microscopy reveals that disruption of ciliary transition-zone architecture causes Joubert syndrome. *Nat. Cell Biol.* **19**, 1178–1188. https://doi.org/10.1038/ncb3599 (2017).
36. Hazime, K. S. et al. STORM imaging reveals the spatial arrangement of transition zone components and IFT particles at the ciliary base in Tetrahymena. *Sci. Rep.* **11**, 7899. https://doi.org/10.1038/s41598-021-86909-5 (2021).
37. Rodgers, L. S., Beam, M. T., Anderson, J. M. & Fanning, A. S. Epithelial barrier assembly requires coordinated activity of multiple domains of the tight junction protein ZO-1. *J. Cell Sci.* **126**, 1565–1575. https://doi.org/10.1242/jcs.113399 (2013).
38. Sun, S. & Zhou, J. Phase separation as a therapeutic target in tight junction-associated human diseases. *Acta. Pharmacol. Sin.* **41**, 1310–1313. https://doi.org/10.1038/s41401-020-0470-y (2020).
39. Rodriguez-Fraticelli, A. E., Galvez-Santisteban, M. & Martin-Belmonte, F. Divide and polarize: recent advances in the molecular mechanism regulating epithelial tubulogenesis. *Curr. Opin. Cell. Biol.* **23**, 638–646. https://doi.org/10.1016/j.ceb.2011.07.002 (2011).
40. Vroman, B. & LaRusso, N. F. Development and characterization of polarized primary cultures of rat intrahepatic bile duct epithelial cells. *Lab. Invest.* **74**, 303–313 (1996).

Acknowledgements

We thank our colleague I.Garcin for her expertise in microscopy. The present work has benefited from Imagerie-Gif core facility supported by l'Agence Nationale de la Recherche (ANR-10-INBS-04/FranceBioImaging ; ANR-11-IDEX-0003-02/ Saclay Plant Sciences). Experimental workflow figures were created with Biorender.com.

Author contributions

PDW designed the project and supervised the work. The experimental work was performed by CCB with the support of LB for cyst 'experiments. CCB made up the figures. CCB and PDW wrote the manuscript. All the authors accepted the manuscript. Supported by Doctoral school Programme blanc GS-Life Science and Health funding.

Funding

INSERM. ANR AAPG2022 PerChol.

Declarations

Competing interests
The authors declare no competing interests.

Additional information
Supplementary Information The online version contains supplementary material available at https://doi.org/10.1038/s41598-024-75577-w.

Correspondence and requests for materials should be addressed to P.D.-W.

Reprints and permissions information is available at www.nature.com/reprints.

Publisher's note Springer Nature remains neutral with regard to jurisdictional claims in published maps and institutional affiliations.